Effect of metallic and hyperbolic metamaterial surfaces on electric and magnetic dipole emission transitions

**X. Ni · G.V. Naik · A.V. Kildishev · Y. Barnakov ·
A. Boltasseva · V.M. Shalaev**

Abstract Spontaneous emission patterns of electric and magnetic dipoles on different metallic surfaces and a hyperbolic metamaterial (HMM) surface were simulated using the dyadic Green's function technique. The theoretical approach was verified by experimental results obtained by measuring angular-dependent emission spectra of europium ions on top of different films. The results show the modified behavior of electric and magnetic dipoles on metallic and HMM surfaces. The results of numerical calculations agree well with experimental data.

1 Introduction

Artificially tailored plasmonic metamaterials are now drawing a significant amount of research interest because of their unique electromagnetic properties that cannot be observed in any naturally occurring materials. The rationally designed properties of these metamaterials enable many fascinating applications, including negative refractive index materials [1], metamaterial antennas [2, 3], subwavelength-resolution imaging [4, 5], and optical cloaking [6, 7].

X. Ni (✉) · G.V. Naik · A.V. Kildishev · A. Boltasseva ·
V.M. Shalaev
Birck Nanotechnology Center, School of Electrical and Computer Engineering, Purdue University, West Lafayette, IN 47907, USA
e-mail: xni@purdue.edu

Y. Barnakov
Center for Materials Research, Norfolk State University, Norfolk, VA 23504, USA

A. Boltasseva
DTU Fotonik, Technical University of Denmark, 2800 Kongens Lyngby, Denmark

Of great interest are metamaterials with hyperbolic dispersion [8, 9], or hyperbolic metamaterials (HMMs) in which different elements of the dielectric tensor have different signs. This class of metamaterials enables sub-wavelength imaging in devices such as the hyperlens [5, 10, 11].

Many of these metamaterial-based devices require complicated setups (often involving near-field detection) to study the field distribution patterns in the vicinity of these metamaterials. However, a simple approach to this problem is to place an electric/magnetic dipole probe near the metamaterial and observe its far-field radiation.

Spontaneous emission of light is one useful process that plays an essential role in many phenomena of light–matter interaction. Spontaneous emission characteristics (including the lifetime, quantum yield, and radiation pattern) are determined not only by the wave functions of the atomic states, but also by the local density of photonic states, which can be greatly affected by the surrounding environment [12–17].

Rare-earth ions exhibiting strong magnetic and electric dipole transitions are good candidates for probing the metamaterials. Europium ions show magnetic and electric dipole dominated transitions at approximately 592 nm (corresponds to the $^5D_0 \rightarrow {}^7F_1$ transition) and 614 nm (corresponds to the $^5D_0 \rightarrow {}^7F_2$ transition), respectively [18]. Efficient excitation of both of these transitions is possible with a chelate system around Eu^{3+} formed by bidentate bipyridyl ligands [19]. Because both of these transitions are relatively strong, well resolved, and can be excited simultaneously in the chelate complex using a UV source of 310 nm, Eu^{3+} ions are good candidates for probing metamaterials.

In an effort to realize this goal, we place bis(2,2′-bipyridyl)-europium nitrate molecules on top of metal and metamaterial surfaces and study their fluorescence patterns. Specifically, we study the effect of near-field inter-

actions of the fluorescent Eu molecule with silver, gold, and HMM surfaces and provide a theoretical framework based on the dyadic Green's function technique to explain the observations. A comparison of the experimental data and the theoretical results is presented to validate the theory.

2 Theoretical model

Theoretical models have been developed to study the emission of Eu^{3+} ions on material surfaces [20, 21]. However, these considered only the far field radiated from the dipoles. Actually, it is very important to take into account the near-field interaction between the dipole molecules and material interfaces. In this paper, we developed an approach that analyzes both near-field and far-field interactions between dipoles and interfaces. We consider a general problem schematically shown in Fig. 1, where a dipole of moment $\mathbf{p}$ with an arbitrary orientation is placed at a subwavelength distance above a multilayer structure. In order to simplify the calculation, we make the position of the dipole coincide with the origin of the global coordinate system. The ith planar interface is located at $z = z_i$ with $i = \overline{1, M+1}$. The material property of the ith layer is characterized by the relative permittivity ε_i and relative permeability μ_i.

The structure is divided into two regions: (1) the semi-infinite host medium where the dipole is embedded and (2) the multilayer structure below the dipole. We expand the electromagnetic field generated by the dipole in terms of the angular spectrum representation in region (1). To begin, we consider an oscillating electric dipole having moment $\mathbf{p}(t) = \mathbf{p}_0 e^{-\iota\omega t}$ ($\iota^2 = -1$) located at $\mathbf{r} = \mathbf{r}_0$. The time-dependent term $e^{-\iota\omega t}$ is omitted throughout the rest of this paper. We use the following expression for the current density of the dipole:

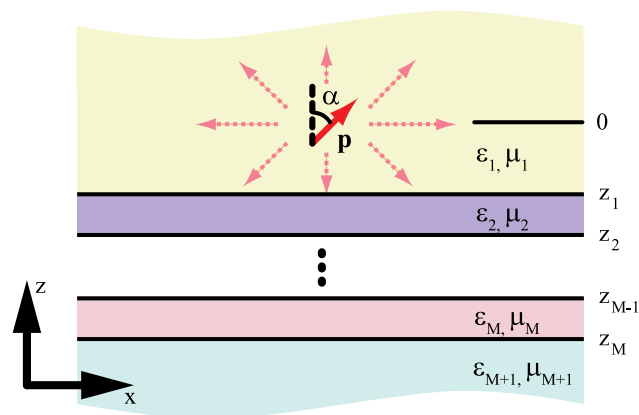$$\mathbf{J}(\mathbf{r}) = -\iota\omega\delta(\mathbf{r} - \mathbf{r}_0)\mathbf{p}_0. \tag{1}$$

Fig. 1 Schematic view of the problem: the dipole is over a multilayer structure

We then obtain the wave equation in the host region

$$(\nabla^2 + k_1^2)\mathbf{E} = -\iota k_1 z_1 \mathbf{J}, \tag{2}$$

where $k_1 = \omega\sqrt{\mu_1\varepsilon_1}$ and $z_1 = \sqrt{\mu_1/\varepsilon_1}$.

In order to obtain the electric field in the upper space of the multilayer structure, we use the dyadic Green's function technique [22–24]. The following form of the dyadic Green's function is used in this paper:

$$\overset{\leftrightarrow}{\mathbf{G}}(\mathbf{r}, \mathbf{r}') = \frac{\iota}{8\pi^2} \int_{-\infty}^{\infty} \int_{-\infty}^{\infty} (\overset{\leftrightarrow}{\mathbf{M}}^s + \overset{\leftrightarrow}{\mathbf{M}}^p) e^{\iota\mathbf{k}\cdot(\mathbf{r}-\mathbf{r}')} dk_x dk_y \tag{3}$$

with

$$\overset{\leftrightarrow}{\mathbf{M}}^s = \frac{1}{k_z k_\rho^2} \begin{pmatrix} k_y^2 & -k_x k_y & 0 \\ -k_x k_y & k_x^2 & 0 \\ 0 & 0 & 0 \end{pmatrix},$$

$$\overset{\leftrightarrow}{\mathbf{M}}_\mp^p = \frac{1}{k^2 k_\rho^2} \begin{pmatrix} k_x^2 k_z & k_x k_y k_z & \mp k_x k_\rho^2 \\ k_x k_y k_z & k_y^2 k_z & \mp k_y k_\rho^2 \\ \mp k_x k_\rho^2 & \mp k_y k_\rho^2 & k_\rho^4/k_z \end{pmatrix}, \tag{4}$$

where $k_\rho = \sqrt{k_x^2 + k_y^2}$. We note that the superscript p or s denotes the values for p-polarized wave (electric field is in the observation plane) or s-polarized wave (electric field is perpendicular to the observation plane). We use a '$-$' sign in $\overset{\leftrightarrow}{\mathbf{M}}_\mp^p$ for the upper half-space and a '$+$' sign for the lower half-space. To calculate the dipole's reflected field, we can multiply the individual plane waves in $\overset{\leftrightarrow}{\mathbf{G}}$ with the corresponding Fresnel reflection coefficients, r^s and r^p, of the multilayer structure, which can be obtained by the transfer matrix method. For the reflected field, we also have the dyadic Green's function

$$\overset{\leftrightarrow}{\mathbf{G}}_r(\mathbf{r}, \mathbf{r}') = \frac{\iota}{8\pi^2} \int_{-\infty}^{\infty} \int_{-\infty}^{\infty} (\overset{\leftrightarrow}{\mathbf{M}}_r^s + \overset{\leftrightarrow}{\mathbf{M}}_r^p) e^{\iota\mathbf{k}\cdot(\mathbf{r}-\mathbf{r}')} dk_x dk_y, \tag{5}$$

where

$$\begin{aligned} \overset{\leftrightarrow}{\mathbf{M}}_r^s &= r^s(k_x, k_y)\overset{\leftrightarrow}{\mathbf{M}}^s, \\ \overset{\leftrightarrow}{\mathbf{M}}_r^p &= -r^p(k_x, k_y)\overset{\leftrightarrow}{\mathbf{M}}_-^p. \end{aligned} \tag{6}$$

The total electric field in the upper half-space can be expressed as

$$\mathbf{E}(\mathbf{r}) = \omega^2 \mu_0 \mu_r [\overset{\leftrightarrow}{\mathbf{G}}(\mathbf{r}, \mathbf{r}_0) + \overset{\leftrightarrow}{\mathbf{G}}_r(\mathbf{r}, \mathbf{r}_0)]\mathbf{p}_0. \tag{7}$$

The Green's function in the far-field zone can be written as [25]

$$\overset{\leftrightarrow}{\mathbf{G}}_{r,\infty}(\mathbf{r}, \mathbf{r}') = \frac{e^{\iota k_1 r}}{4\pi r} (\overset{\leftrightarrow}{\mathbf{M}}_{r,\infty}^s + \overset{\leftrightarrow}{\mathbf{M}}_{r,\infty}^p) e^{-\iota k_1(x_0 x/r + y_0 y/r - z_0 z/r)}, \tag{8}$$

where

$$\overset{\leftrightarrow}{\mathbf{M}}{}^{\mathrm{s}}_{\mathrm{r},\infty} = \frac{r^{\mathrm{s}}}{\rho^2} \begin{pmatrix} y^2 & -xy & 0 \\ -xy & x^2 & 0 \\ 0 & 0 & 0 \end{pmatrix},$$

$$\overset{\leftrightarrow}{\mathbf{M}}{}^{\mathrm{p}}_{\mathrm{r},\infty} = \frac{r^{\mathrm{p}}}{r^2} \begin{pmatrix} x^2 z^2/\rho^2 & xyz^2/\rho^2 & xz \\ xyz^2/\rho^2 & y^2 z^2/\rho^2 & yz \\ -xz & -yz & -\rho^2 \end{pmatrix}, \tag{9}$$

where $\rho = \sqrt{x^2 + y^2}$.

In the far field, the time-averaged Poynting vector can be expressed as

$$\langle \mathbf{S} \rangle = \frac{1}{2}\mathrm{Re}\{\mathbf{E}_\infty \times \mathbf{H}^*_\infty\} = \frac{1}{2}z_0^{-1}z_{\mathrm{r}}^{-1}|\mathbf{E}|^2\hat{\mathbf{r}}, \tag{10}$$

where $\hat{\mathbf{r}}$ is the unit vector in the radial direction. The radiated power density (P) per solid angle $\mathrm{d}\Omega = \sin\theta\,\mathrm{d}\theta\,\mathrm{d}\phi$ is given by

$$P = p(\theta, \phi)\,\mathrm{d}\Omega = r^2\langle \mathbf{S} \rangle\hat{\mathbf{r}}. \tag{11}$$

The normalized radiation power for s- and p-polarizations can be written as

$$\frac{p^{\mathrm{s}}(\theta, \phi)}{P_0} = \frac{3}{8\pi}\frac{1}{|\mathbf{p}|^2}(p_x\sin\phi - p_y\cos\phi)^2|1 + r^{\mathrm{s}}|^2,$$

$$\frac{p^{\mathrm{p}}(\theta, \phi)}{P_0} = \frac{3}{8\pi}\frac{1}{|\mathbf{p}|^2}\{p_z^2\sin^2\theta|1 + r^{\mathrm{p}}|^2$$

$$+ (p_x\cos\phi + p_y\sin\phi)^2\cos^2\theta|1 - r^{\mathrm{p}}|^2$$

$$- p_z(p_x\cos\phi + p_y\sin\phi)\cos\theta\sin\theta$$

$$\times\left[(1 + r^{\mathrm{p}})^*(1 - r^{\mathrm{p}}) + (1 + r^{\mathrm{p}})(1 - r^{\mathrm{p}})^*\right]\}, \tag{12}$$

where P_0 is the total rate of energy dissipation, which is calculated using

$$P_0 = \frac{|\mathbf{p}|^2}{4\pi\varepsilon_0\varepsilon_{\mathrm{r}}}\frac{n^3\omega^4}{3c^3}. \tag{13}$$

According to the electric–magnetic duality, the radiation pattern for the magnetic dipole with moment $\mu\mathbf{p}$ can be obtained by doing the following substitution:

$$(\mathbf{E}, \mathbf{H}, \mu, \varepsilon, r^{\mathrm{s}}, r^{\mathrm{p}}) \rightarrow (\mathbf{H}, -\mathbf{E}, \varepsilon, \mu, r^{\mathrm{p}}, r^{\mathrm{s}}). \tag{14}$$

Using the theoretical scheme above, the electromagnetic field radiated by the electric/magnetic dipoles can be calculated in the far-field zone. Experiments were conducted to validate the scheme.

3 Experiment

Three different samples were prepared for the experiment as shown in Fig. 2: a polymer film containing the europium complex coated on top of gold, silver, and silver–alumina multilayer stacks.

On clean glass substrates, metal/dielectric layers were evaporated via e-beam, yielding three different samples with: 300-nm-thick gold, 500-nm-thick silver, and 16 alternating layers of gold and alumina, each 20-nm thick. The thicknesses of the evaporated layers were monitored carefully during deposition by a quartz crystal microbalance and confirmed later by a profilometer (KLA-Tencor alpha-step profilometer). These substrates were spin coated to form about 75-nm-thick films consisting of [Eu(2,2′-bipyridyl)$_2$](NO$_3$)$_3$ in polyvinylpyrrolidone (PVP 8 kDa, purchased from Alfa-Aesar) (10 wt.%) as described elsewhere [21]. The synthesis of crystals of [Eu(2,2′-bipyridyl)$_2$](NO$_3$)$_3$ was carried out by slow evaporation of ethanol solution of europium(III) nitrate and 2,2′-bipyridyl mixed in 1:2 molar ratio at room temperature [19, 26]. Adhesion of the PVP:Eu-complex thin film onto the metal surface was promoted by an ultra-thin layer (about 6–8 nm) of mercaptoundecanoic acid (MUA), which was formed on the metal surface prior to the spin coating of the PVP:Eu-complex film. The MUA layer also served as a protecting layer for silver films from mildly corrosive ethanol solution of [Eu(2,2′-bipyridyl)$_2$](NO$_3$)$_3$. The film thicknesses of europium complex and MUA were measured by a profilometer (KLA-Tencor alpha-step profilometer) and an atomic force microscope (AFM Veeco Dimension).

The fluorescence measurements of the thin films were carried out using a Varian Eclipse Cary fluorescence spectrophotometer. The characterization setup is shown in Fig. 3. A custom setup for mounting thin-film samples on a rotatable goniometer stage was built. The observation angle θ was defined as the angle between the detector and the sample plane (see Fig. 3). An optical slit was inserted between the sample and the photomultiplier tube (PMT) to narrow the observation angle. A linear polarizer was inserted in front of the slit to select s-/p-polarization. Appropriate filters were
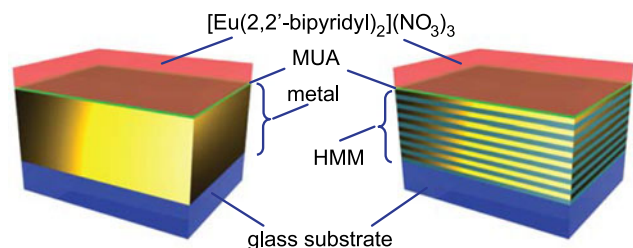

Fig. 2 Schematic view of the samples: metallic film sample (*left*) and HMM sample (*right*)
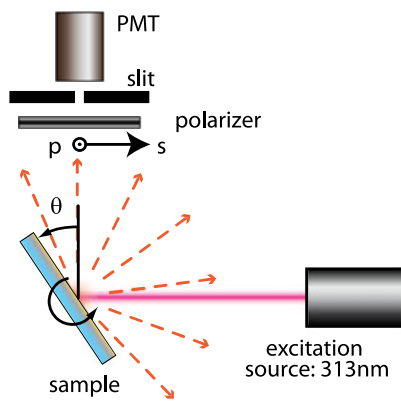
Fig. 3 Fluorescence characterization experimental setup

Fig. 4 Typical spontaneous emission spectra of Eu^{3+} ions at the observation angle of 45 degrees for s- and p-polarizations normalized to the transition at 617 nm

Table 1 Optimized fitting parameters in the calculations

Sample	t_g (nm)	t_s (nm)	γ_e (594 nm)	γ_e (617 nm)
Gold	67.9	6	0.22	0.75
Silver	67	8	0.21	0.72
HMM	64.5	8	0.2	0.7

used at detector and source to allow detection in the wavelength range of 550–650 nm and excitation at a wavelength of 313 nm.

4 Results and discussion

The photoluminescence spectra of Eu^{3+} at $\theta = 45°$ with different polarizations are shown in Fig. 4. The dominating emission peaks at 594 nm and 617 nm can be ascribed to the $^5D_0 \rightarrow {}^7F_1$ magnetic dipole transition and to the $^5D_0 \rightarrow {}^7F_2$ electric dipole transition, respectively [18]. The positions of the peaks are slightly different from predictions due to different synthesis conditions.

The characterization setup was not able to measure the angular radiation pattern because the incident angle of the excitation beam was changing with the observation angle θ. Therefore, the excitation power was not held constant. However, at each observation angle, the intensity ratio of the electric and magnetic dipole radiation peaks was not the same at different polarizations. For example, Fig. 4 shows that the magnetic dipole radiation peak was suppressed in s-polarization. Therefore, rather than comparing the angular radiation pattern, we can compare the angular-dependent quantity—which is the ratio of the radiation intensities at wavelengths of 594 nm and 617 nm ($I(\lambda = 594\text{ nm})/I(\lambda = 617\text{ nm})$).

The angular-dependent emission intensity ratios for the Eu^{3+} ions on gold film, silver film, and HMM are shown in Fig. 5, respectively. The dots in the figures are the measured data points, and the solid lines are the calculated data. The shaded areas in the figures indicate relatively poor experimental accuracy, because of nearly grazing angles of incidence or observation. The dielectric constants of silver and gold were obtained from the literature [27] and also are available in an online tool [28]. The radiation was averaged over different orientations of the dipoles and was integrated over the thickness of the Eu-complex:PVP layer. The thicknesses of the Eu-complex:PVP layer (t_g) and the MUA layer
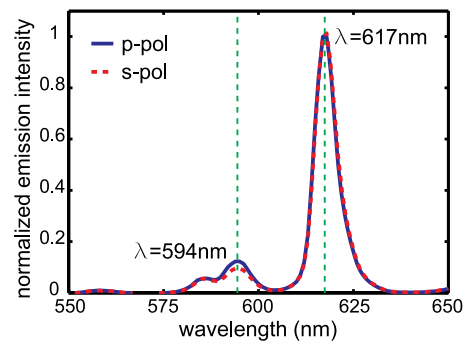
(t_s) and the fractional contribution to the fluorescence originating from electric dipole transitions ($\gamma_e(\lambda)$, also referred to as a contribution factor) and magnetic dipole transitions ($\gamma_m(\lambda) = 1 - \gamma_e(\lambda)$) of each peak were tuned using a genetic algorithm and a pattern search algorithm. This procedure was used to match the calculated data to the experimental results, where the contribution factors were introduced due to the fact that both 594-nm and 617-nm emission peaks of Eu^{3+} originate from a mixture of electric dipole and magnetic dipole transitions. The radiated intensity can be expressed as

$$I(\lambda) = \gamma_e(\lambda)I_e(\lambda) + \gamma_m(\lambda)I_m(\lambda). \qquad (15)$$

The optimized parameters used in calculations are shown in Table 1. The dimensions are within the range of the values obtained from sample characterization and the contribution factors for both the wavelengths of 594 nm and 617 nm are reasonable compared to those in the literature [21].

From Fig. 5a and b, we can see that the calculation results match reasonably well with the experimental data for Eu^{3+} on gold and silver films. The slight discrepancy comes from the measurement errors, including inaccuracy of observation angle, background noise, and averaging effect over the optical slit width. From Fig. 5c, we can see the calculated and measured results do not match as well as the previous ones. This is most likely because of the imperfection of the HMM sample due to the fabrication processes (including surface roughness, small mean grain size of the metal, which profoundly influences its dielectric function, non-uniformity of each metal layer, and the difference in the thicknesses of the actual layers and the ideal design layers).
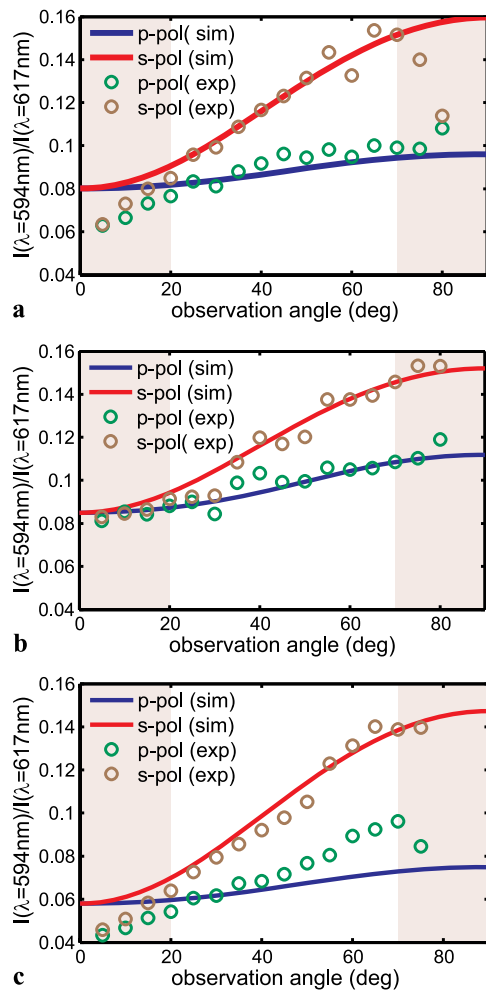
Fig. 5 Angular-dependent emission intensity ratios $I(\lambda = 594 \text{ nm})/I(\lambda = 617 \text{ nm})$ for s- and p-polarizations of Eu^{3+} ions on (**a**) gold film sample, (**b**) silver film sample, and (**c**) HMM sample

from experiments matches the calculated results reasonably well, validating the theoretical approach. This also confirms that the fluorescence peaks at 594 nm and 617 nm are predominantly from magnetic dipole and electric dipole transitions, respectively. The small discrepancies between the experiments and the theory are mainly due to the limitations of the experimental setup, imperfection of the samples, and random errors during the measurement process. The measurement accuracy can be improved by using better samples and a fully customized experimental setup. For example, the setup could have a fixed sample stage and excitation source, and a rotatable detector which rotates around the sample, performing the radiation pattern measurement.

Further studies of the effects of the metamaterial surface in the vicinity of the Eu^{3+} ion on the electric and magnetic dipole transitions are in progress. These include the study of the radiation pattern of the dipoles on negative-index metamaterials, and fluorescence lifetime changes in the presence of metamaterials.

The results show that the behaviors of the spontaneous emission of electric and magnetic dipoles are different in the presence of a metallic surface or an HMM surface, as can be distinguished by the angular-dependent radiation measurement (splitting of s-/p-polarization curves). This enables potential applications in the field of sensing.

5 Summary

We used a classical approach to study the behavior of electric and magnetic dipoles located at a subwavelength distance above a material surface. Three different sample designs: Eu^{3+} on a silver film, Eu^{3+} on a gold film, and Eu^{3+} on a hyperbolic metamaterial (HMM) were investigated. These three samples were fabricated and characterized for the fluorescence spectrum of the Eu^{3+} ion. The angular dependence of the ratio of the fluorescence-peak intensities at 594-nm and 617-nm wavelengths measured

References

1. V.M. Shalaev, Nat. Photonics **1**, 41 (2007)
2. S. Enoch, G. Tayeb, P. Sabouroux, N. Guerin, P. Vincent, Phys. Rev. Lett. **89**, 213902 (2002)
3. K.B. Alici, E. Ozbay, Phys. Status Solidi (b). Basic Solid State Phys. **244**, 1192 (2007)
4. J.B. Pendry, Phys. Rev. Lett. **85**, 3966 (2000)
5. Z. Jacob, L.V. Alekseyev, E. Narimanov, Opt. Express **14**, 8247 (2006)
6. J.B. Pendry, D. Schurig, D.R. Smith, Science **312**, 1780 (2006)
7. W.S. Cai, U.K. Chettiar, A.V. Kildishev, V.M. Shalaev, Opt. Express **16**, 5444 (2008)
8. J. Yao, Z.W. Liu, Y.M. Liu, Y. Wang, C. Sun, G. Bartal, A.M. Stacy, X. Zhang, Science **321**, 930 (2008)
9. M.A. Noginov, Y.A. Barnakov, G. Zhu, T. Tumkur, H. Li, E.E. Narimanov, Appl. Phys. Lett. **94**, 151105 (2009)
10. Z. Jacob, L.V. Alekseyev, E. Narimanov, in *Conf. Lasers & Electro-Optics/Quantum Electronics and Laser Science Conf. (Cleo/Qels 2007)* (2007), p. 2095, vols. 1–5
11. A.V. Kildishev, U.K. Chettiar, Z. Jacob, V.M. Shalaev, E.E. Narimanov, Appl. Phys. Lett. **94**, 071102 (2009)
12. W.L. Barnes, J. Mod. Opt. **45**, 661 (1998)
13. W. Lukosz, J. Opt. Soc. Am. **69**, 1495 (1979)
14. P. Andrew, W.L. Barnes, Phys. Rev. B **64**(12), 125405 (2001)
15. L. Novotny, B. Hecht, *Principles of Nano-Optics* (Cambridge University Press, Cambridge, 2006)
16. P. Anger, P. Bharadwaj, L. Novotny, Phys. Rev. Lett. **96**, 113002 (2006)
17. S. Karaveli, R. Zia, Opt. Lett. **35**, 3318 (2010)
18. W.T. Carnall, P.R. Fields, K. Rajnak, J. Chem. Phys. **49**, 4450 (1968)
19. N. Noginova, G. Zhu, M. Mavy, M.A. Noginov, J. Appl. Phys. **103**, 07E901 (2008)
20. K.H. Drexhage, Bull. Am. Phys. Soc. **14**, 873 (1969)

21. N. Noginova, Y. Barnakov, H. Li, M.A. Noginov, Opt. Express **17**, 10767 (2009)
22. C.E. Reed, J. Giergiel, J.C. Hemminger, S. Ushioda, Phys. Rev. B **36**, 4990 (1987)
23. K.A. Michalski, J.R. Mosig, IEEE Trans. Antennas Propag. **45**, 508 (1997)
24. J.R. Mosig, A.A. Melcon, IEEE Trans. Antennas Propag. **51**, 3200 (2003)
25. W.C. Chew, *Waves and Fields in Inhomogeneous Media* (Wiley/IEEE Press, New York, 1999)
26. V. Tsaryuk, K. Zhuravlev, V. Zolin, V. Kudryashova, J. Legendziewicz, R. Szostak, J. Appl. Spectrosc. **74**, 51 (2007)
27. P.B. Johnson, R.W. Christy, Phys. Rev. B **6**, 4370 (1972)
28. X. Ni, Z. Liu, A.V. Kildishev, doi:10254/nanohub-r3692.10 (2007)